The Integrated Reference Region Analysis for Parallel DFIGs' Interfacing Inductors

Rui Wang, *Member, IEEE,* Xiaohan Yu, Qiuye Sun, *Senior Member, IEEE,* Dashuang Li, *Student Member, IEEE,* Yonghao Gui, *Senior Member, IEEE,* and Peng Wang, *Fellow, IEEE*

***Abstract*—Although the traditional design of doubly-fed induction generators (DFIGs)' interfacing inductors consider the peak ripple of the grid-side converter (GSC)'s output current, it does not consider the inductors' impact on DFIGs' small-signal stability. Located in series between the GSC and the stator, the inappropriate selection of the interfacing inductor can easily result to system instability. Therefore, this paper first proposes the integrated reference region analysis for small wind farm's interfacing inductors to improve the traditional design method. Firstly, a new detailed parallel DFIGs' small-signal model that considers output currents' coupling is built in d-q coordinate system with state-space approach. The model focuses on representing the operating states of parallel DFIGs in wind farm. Secondly, the linearized state-space matrix of parallel DFIGs is decomposed into nominal-value matrix and location matrix. Considering the traditional design requirements, the integrated reference region for interfacing inductor is proposed through spectral radius and bialternate matrix sum (BMS). It can provide better guidance for parameter selecting and stabilization method researches. Finally, the simulation and experimental results show that the proposed integrated reference region for parallel DFIGs' interfacing inductors is accurate and instructive.**

***Index Terms*—integrated reference region analysis, interfacing inductor, parallel DFIGs, small-signal modeling, small-signal stability**

I. Introduction

GLOBALLY, 77.6 GW of wind power capacity was added in 2022 [1]. As the scale of doubly-fed induction generators (DFIGs) connected to the grid grows, small-signal instability, including sub/super-synchronous oscillation, low frequency oscillation, Etc, is more prone to occur and even more urgent to be solved in the power system with high penetration of power electronics [2], compared to the transient instability. Additionally, the interfacing inductor of DFIG also likely causes small-signal instability [3], which locates in series with the Grid-Side Converter (GSC) and stator. However, the traditional reference value design method of the inductor is usually calculated through allowable current ripple and the maximum output current of GSC [4], it doesn't consider the small-signal stability of the system. Therefore, the impact of DFIG's interfacing inductor on small-signal stability and the stability region for this inductor are of great significance to be studied.

On one hand, the design of interfacing inductors is particularly important in power electronics and converters. As presented in literature [5], a properly designed interfacing inductor in filter should consider minimum voltage drop across the filter, minimum stored energy, improved damping performance, etc. On this basis, literature [6] proposes an improved efficient design principle. It considers the ratio between the grid-side and inverter-side inductance, type of damping scheme employed, employed control structure and so on. For the effect of the inductors on system's stability, literature [7] proposes a restraint on designing the LCL filter by limiting the resonance frequency within the designed region. Nevertheless, literature [8] demonstrates that the resonance frequency of the filter might still shift out of the designed region. Thus, a time delay compensating method in the control loop is proposed to broaden the designed region [9]. Still, the compensating method decreases the filter's bandwidth and deteriorates its dynamic performance, as presented in literature [10]. So far, the main designing consideration is to increase the resonance frequency by adding compensation and to improve the control loop to suppress the oscillation in the inductors and filters. Similarly, the interfacing inductors in DFIGs are designed upon allowable current ripple and maximum output current of GSC. Most of the existing methods concentrates on the compensation of system's stability for a certain inductor that satisfies the current ripple requirement. There is still a lot of blank space to analyze the effect of inductors on system's stability and to improve the design.

On the other hand, the commonly used methods in studying the system's stability issue includes impedance method and state space method [11]-[15]. For impedance method, literature [16] proposes an impedance model of type 3 DFIG-based wind generator to analyze the leading cause of the sub-synchronous resonance oscillation. Literature [17] analyzes the cause of the high frequency resonance phenomenon based on the high-frequency impedance model and proposes an impedance reshaping control strategy to weaken the frequency coupling phenomenon. The impedance method has great advantages in

This work is supported by the National Key Research and Development Program of China under Grant 2018YFA0702200, in part by the China Postdoctoral Science Foundation Funded Project under Grant ZX20210282, in part by the Fundamental Research Funds for the Central Universities in China under Grant N2204014, in part by the Guangdong Basic and Applied Basic Research Foundation under Grant 2021A1515110915, and in part by the National Natural Science Foundation of China under Grant U20A20190 and Grant 52307194. (Corresponding authors: Qiuye Sun.)

Rui Wang, Xiaohan Yu, Qiuye Sun and Dashuang Li are with the Northeastern University, Shenyang, Liaoning 110819, China (e-mail: wangrui@ise.neu.edu.cn; 2310261@stu.neu.edu.cn; sunqiuye@ise.neu.edu.cn; 2210276@stu.neu.edu.cn).

Yonghao Gui is with the Oak Ridge National Laboratory, Electrification and Energy Infrastructures Division, TN 37932, US (e-mail:y.gui@ieee.org)

Peng Wang is with the School of Electrical and Electronic Engineering, Nanyang Technological University Singapore 639798, Singapore (e-mail:epwang@ntu.edu.sg).

representing the overall characteristics of the system. However, it mainly focuses on explaining the cause of system oscillation, which can't intuitively analyze the effect of a particular parameter on system's stability. In contrast, the state-space method is more intuitive in modeling and system's stability analysis on parameters. Literature [18] uses state-space model to analyze the phase-locked loop (PLL)'s impact on DFIG system's instability during weak grid fault and proposes a new low-voltage ride through strategy. Literature [19] investigates the dominant unstable poles' influence factors during asymmetric faults and proposes an oscillation suppressing control algorithm. At present, most of the models established are based on a single DFIG, when the state-space method is applied to analyze the influence of specific parameters on the system's stability. However, for complex and high-order systems, it is tedious to establish the corresponding state-space model to represent the overall characteristics of the system. Therefore, it is urgent to propose an analytical method that can not only effectively represent the overall characteristics of a complex system, but also intuitively analyze the influence of specific parameters on system's stability.

To fill this gap, the integrated reference region analysis for parallel DFIGs' interfacing inductors based on the BMS is first proposed in this paper. The main advantages are shown as follows.

1) For the first time, a detailed state-space model of parallel DFIGs based on wind turbines is proposed. It focuses more on representing the operating states of DFIGs in small wind farm and considers the coupling of output currents on the common transmission line, which is helpful to reflect the overall characteristics of small wind farm.

2) The integrated reference region of parallel DFIGs' interfacing inductors is first introduced through BMS which uses the derivatives of parallel DFIGs' state-space matrix for computation, taking account of current ripple requirement and system's small-signal stability. It can provide guidance for system stabilization and parameter selection.

The paper structure is as follows: Section II describes the parallel DFIGs' system and establishes each part of the system model. On this basis, section III introduces a mathematical method of BMS to get the integrated reference region for DFIGs' interfacing inductors from the state-space model. The corresponding simulation and experimental results are provided in Section IV and Section V respectively. Section VI concludes the work.

II. Small-Signal Model of Parallel DFIGs

The parallel DFIGs system studied in this paper consists of n parallel DFIGs. It is shown in Fig. 1. As a matter of fact, the wind farm is an intricate system integrated with plenty of converters, transformers, energy storages and loads. Modeling all system devices at the same time is unpractical. Therefore, the number of parallel DFIGs is chosen as two, which can represent the whole system effectively. The following consists of different parts' modeling of the parallel DFIGs' system with coupling, which includes the mechanical part, control part, interfacing inductor and transmission line coupling.

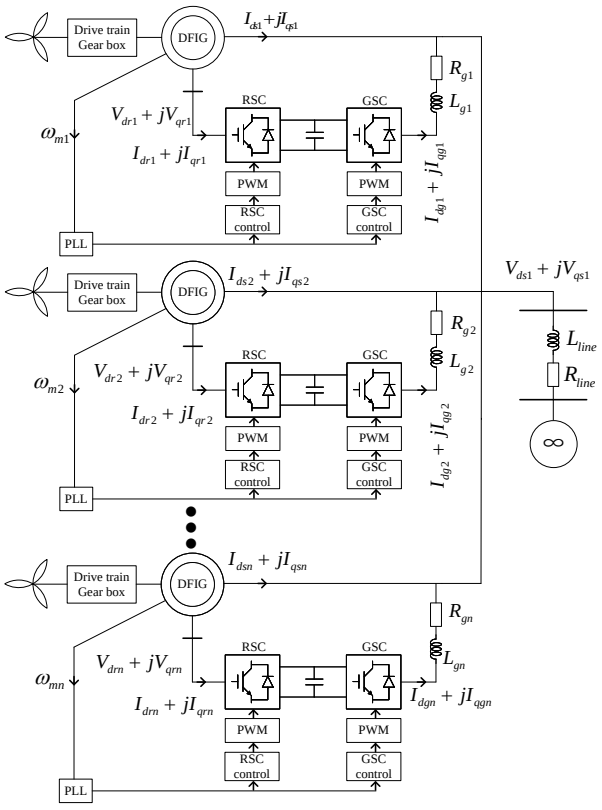

Fig. 1. Coupled parallel doubly-fed induction generator model

A. Turbine Model

A common reference frame that rotates synchronously with the stator voltage vector is formed. The currents are selected as state variables for simpler model expression and convenient control. For balanced and unsaturated conditions, the electrical equations of stator and rotor circuits are as follows [20]

$$\begin{cases} V_{ds} = R_s \cdot i_{ds} - \omega_s \cdot \psi_{qs} + \frac{d\psi_{ds}}{dt} \\ V_{qs} = R_s \cdot i_{qs} + \omega_s \cdot \psi_{ds} + \frac{d\psi_{qs}}{dt} \\ V_{dr} = R_r \cdot i_{dr} - s \cdot \omega_s \cdot \psi_{qr} + \frac{d\psi_{dr}}{dt} \\ V_{qr} = R_r \cdot i_{qr} + s \cdot \omega_s \cdot \psi_{dr} + \frac{d\psi_{qr}}{dt} \end{cases} \tag{1}$$

The flux equation of a DFIG can be expressed as

$$\begin{cases} \psi_{ds} = L_s \cdot i_{ds} + L_m \cdot i_{dr} \\ \psi_{qs} = L_s \cdot i_{qs} + L_m \cdot i_{qr} \\ \psi_{dr} = L_r \cdot i_{dr} + L_m \cdot i_{ds} \\ \psi_{qr} = L_r \cdot i_{qr} + L_m \cdot i_{qs} \end{cases} \tag{2}$$

Substitute Equation (2) into equation(1) and linearize to obtain (3), where $|\bullet|_0$ is the steady operating state value of $|\bullet|$, V_{ds} and V_{qs} are the stator voltages of d and q axis accordingly, R_s is the stator resistance, ψ_{ds} and ψ_{qs} are the stator flux of d and q axis accordingly, V_{dr} and V_{qr} are the rotor voltages of d and q axis respectively, R_r is the rotor resistance, ψ_{dr} and ψ_{qr} are the rotor flux of d and q axis accordingly, i_{ds} and i_{qs} are stator current of d and q axis respectively, i_{dr} and i_{qr} are stator current of d and q axis accordingly, L_s and L_r are the inductances of the stator and rotor accordingly, L_m is

$$\begin{cases} \dfrac{d\Delta i_{ds}}{dt} = -\dfrac{1}{L_sL_r - L_m^2}[-(L_mL_ri_{qr0} + L_m^2 i_{qs0})\Delta\omega_m + \omega_s(s_0L_m^2 - L_sL_r)\Delta i_{qs} + \omega_sL_mL_r(s_0-1)\Delta i_{qr} \\ \qquad + L_rR_s\Delta i_{ds} - R_rL_m\Delta i_{dr} - L_r\Delta V_{ds} + L_m\Delta V_{dr}] \\ \dfrac{d\Delta i_{qs}}{dt} = -\dfrac{1}{L_sL_r - L_m^2}[(L_mL_ri_{dr0} + L_m^2 i_{ds0})\Delta\omega_m - \omega_s(s_0L_m^2 - L_sL_r)\Delta i_{ds} - \omega_sL_mL_r(s_0-1)\Delta i_{dr} \\ \qquad + L_rR_s\Delta i_{qs} - L_mR_r\Delta i_{qr} - L_r\Delta V_{qs} + L_m\Delta V_{qr}] \\ \dfrac{d\Delta i_{dr}}{dt} = \dfrac{1}{L_sL_r - L_m^2}[-(L_mL_si_{qs0} + L_rL_si_{qr0})\Delta\omega_m + \omega_sL_mL_s(s_0-1)\Delta i_{qs} + \omega_s(s_0L_sL_r - L_m^2)\Delta i_{qr} \\ \qquad + L_mR_s\Delta i_{ds} - R_rL_s\Delta i_{dr} - L_m\Delta V_{ds} + L_s\Delta V_{dr}] \\ \dfrac{d\Delta i_{qr}}{dt} = \dfrac{1}{L_sL_r - L_m^2}[(L_mL_si_{ds0} + L_rL_si_{dr0})\Delta\omega_m - \omega_sL_mL_s(s_0-1)_s\Delta i_{ds} - \omega_s(s_0L_sL_r - L_m^2)\Delta i_{dr} \\ \qquad + L_mR_s\Delta i_{qs} - R_rL_s\Delta i_{qr} - L_m\Delta V_{qs} + L_s\Delta V_{qr}] \end{cases} \tag{3}$$

the magnetizing inductance, and ω_m is the electrical angular velocity of the generator.

B. Drive Train Model

The equation of the DFIG drive train part model can be expressed as

$$\begin{cases} J_1\frac{\mathrm{d}\Omega_1}{\mathrm{d}t} = T_t - K\cdot\theta_t \\ J_2\frac{\mathrm{d}\Omega_2}{\mathrm{d}t} = K\cdot\theta_t - T_{em} \\ \frac{\mathrm{d}\theta_t}{\mathrm{d}t} = \Omega_1 - \Omega_2 \end{cases} \tag{4}$$

where J_1 is the rotational inertia of the low speed shaft, J_2 is the rotational inertia of the high speed shaft, Ω_1 is the wind turbine angular speed, Ω_2 is the generator angular speed, T_t is the input mechanical torque of the wind turbine, T_{em} is the electromagnetic torque of the generator, K is the shaft stiffness, and θ_t is the shaft twist angle.

Since the mechanical part of the wind turbine has little influence on the stability region of electrical part parameters of the DFIG, the drive train part model is simplified as follows

$$J\frac{d\Omega_m}{dt} = T_{t\_ar} - D\cdot\Omega_m - T_{em} \tag{5}$$

The drive train small-signal model can be expressed as

$$J\tfrac{d\Delta\omega_m}{dt} = -\tfrac{D}{J}\cdot\Delta\omega_m + \tfrac{3p^2L_m}{2J}(i_{ds0}\cdot\Delta i_{qr} + i_{qr0}\cdot\Delta i_{ds} - i_{qs0}\cdot\Delta i_{dr} - i_{dr0}\cdot\Delta i_{qs}) \tag{6}$$

where J is the rotational inertia, Ω_m is the mechanical angular velocity of the generator, $T_{t\_ar} = \frac{1}{2}\cdot\frac{\rho\pi R^3V_v^2C_t}{N}$ is the shaft torque, ρ is the air density, R is the radius of the DFIGs' blades, V_v is the average wind speed, C_t is the torque coefficient, N is the gear box ratio, p is the pole pair, D is the damping ratio, and $T_{em} = \frac{3}{2}p\frac{L_m}{L_s}(\psi_{qs}\cdot i_{dr} - \psi_{ds}\cdot i_{qr})$ is the electromagnetic torque.

C. Rotor-Side Control model

The voltage equation can be written out from the rotor side control structure in Fig. 2 as

$$\begin{cases} V_{dr} = kp_{id1}\cdot\frac{dx_1}{dt} + ki_{id1}\cdot x_1 - \omega_r\sigma L_ri_{qr} \\ V_{qr} = kp_{id2}\cdot\frac{dx_2}{dt} + ki_{id2}\cdot x_2 + \omega_r\sigma L_ri_{dr} \\ T_{em} = -\frac{\omega_m^2}{N^3}\cdot\frac{\rho\pi R^5C_{p\_\max}}{2\lambda_{opt}^3} \end{cases} \tag{7}$$

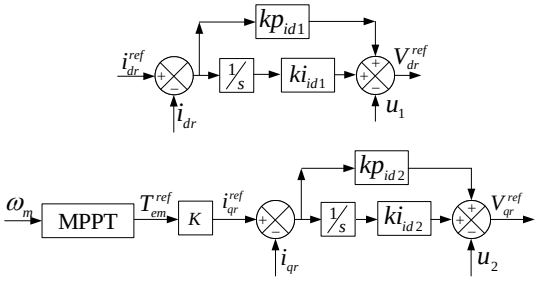

Fig. 2. Rotor-side converter control structure

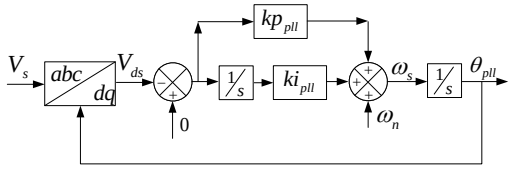

Fig. 3. Phase locked loop structure

The rotor side control small-signal model can be expressed as

$$\begin{cases} \dfrac{d\Delta x_1}{dt} = \dfrac{1}{kp_{id1}}[\Delta V_{dr} + \sigma L_r(s_0\omega_s\Delta i_{qr} - i_{qr0}\Delta\omega_m) - ki_{id1}\Delta x_1] \\ \dfrac{d\Delta x_2}{dt} = \dfrac{1}{kp_{id2}}[\Delta V_{qr} - \sigma L_r(s_0\omega_s\Delta i_{dr} - i_{dr0}\Delta\omega_m) - ki_{id2}\Delta x_2] \\ \Delta i_{qr}^{ref} = -\dfrac{\rho\pi R^5C_p^{\max}\omega_m}{KN^3\lambda_{opt}^3}\Delta\omega_m \end{cases} \tag{8}$$

where $u_1 = \omega_r\sigma L_ri_{qr}$ and $u_2 = -\omega_r\sigma L_ri_{dr}$ are disturbances, $\sigma = 1 - L_m^2/(L_sL_r)$ and $K = -2L_s/(3pL_m\psi_{s0})$ are constants, $\frac{dx_1}{dt} = i_{dr}^{ref} - i_{dr}$, $\frac{dx_2}{dt} = i_{qr}^{ref} - i_{qr}$, $C_p^{\max}$ is the maximum wind energy utilization factor, and λ_{opt} is the optimal tip ratio.

D. Phase-Locked Loop Model

Phase locked loop is the key part of the system transformation from the abc three-phase stationary coordinate to the

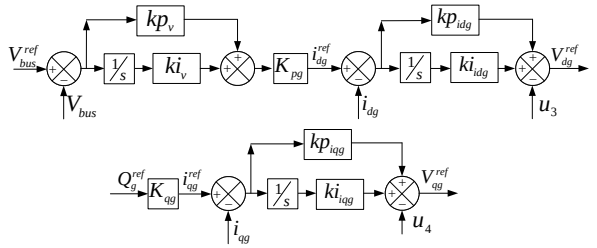

Fig. 4. Grid-side converter control structure

d-q rotational coordinate, besides, the grid voltage orientaion is used in this paper. Its structure is shown in Fig. 3.

The PI controller equation can be written out from the Phase locked loop structure figure as

$$\begin{cases} \frac{d\theta_{pll}}{dt} = kp_{pll} \cdot (-V_{ds}) + ki_{pll} \cdot x_3 \\ \frac{dx_3}{dt} = -V_{ds} \end{cases} \tag{9}$$

The small-signal model of pll can be acquired as

$$\begin{cases} \frac{d\Delta\theta_{pll}}{dt} = -kp_{pll}\Delta V_{ds} + ki_{pll}\Delta x_3 \\ \frac{d\Delta x_3}{dt} = -\Delta V_{ds} \end{cases} \tag{10}$$

where θ_{pll} is the output of the phase locked loop, kp_{pll} is the proportional gain, and ki_{pll} is the integral gain of the PI controller.

E. Grid-Side Control Model

The PI controller equation can be written out from the grid side control structure in Fig. 4 as

$$\begin{cases} kp_v \frac{dx_4}{dt} + ki_v x_4 = k_{pg} i_{dg}^{ref} \\ kp_{idg} \frac{dx_5}{dt} + ki_{idg} x_5 - \omega_r \sigma L_r i_{qr} = V_{dg}^{ref} \\ kp_{iqg} \frac{dx_6}{dt} + ki_{iqg} x_6 + \omega_r \sigma L_r i_{dr} = V_{qg}^{ref} \end{cases} \tag{11}$$

The small-signal model of grid side control can be expressed as

$$\begin{cases} \frac{d\Delta x_5}{dt} = \frac{1}{kp_{idg}}[\Delta V_{dg} + \sigma L_r(s_0\omega_s\Delta i_{qr} - i_{qr0}\Delta\omega_m)] \\ \qquad - ki_{idg}\Delta x_5 \\ \frac{d\Delta x_6}{dt} = \frac{1}{kp_{iqg}}[\Delta V_{qg} + \sigma L_r(i_{dr0}\Delta\omega_m - s_0\omega_s\Delta i_{dr})] \\ \qquad - ki_{iqg}\Delta x_6 \\ \frac{d\Delta x_4}{dt} = \frac{1}{kp_v}(-ki_v\Delta x_4 + k_{pg}\Delta i_{dg}) \end{cases} \tag{12}$$

where $u_3 = \omega_r\sigma L_r i_{qr}$ and $u_4 = -\omega_r\sigma L_r i_{dr}$ are disturbances, $K_{pg} = -K_{qg} = \sqrt{6}/(3V_s)$ are constant coefficients, V_{dg} and V_{qg} are grid-side voltage of d and q axis, i_{dg} and i_{qg} are the grid-side currents of d and q axis respectively, $\frac{dx_4}{dt} = V_{bus}^{ref} - V_{bus}$, $\frac{dx_5}{dt} = i_{dg}^{ref} - i_{dg}$, and $\frac{dx_6}{dt} = i_{qg}^{ref} - i_{qg}$.

F. DC Bus Model

The DC bus model structure is shown in Fig. 5. According to the power balance equation, the model of DC bus can be expressed as

$$\begin{cases} C_{bus}V_{bus}\frac{dV_{bus}}{dt} = P_g - P_r \\ P_g = V_{dg} \cdot i_{dg} + V_{qg} \cdot i_{qg} \\ P_r = V_{dr} \cdot i_{dr} + V_{qr} \cdot i_{qr} \end{cases} \tag{13}$$

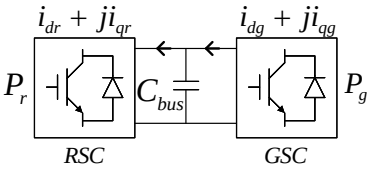

Fig. 5. DC bus model

The small-signal model of DC bus can be acquired as

$$\begin{aligned} \frac{d\Delta V_{bus}}{dt} = &-\frac{1}{C_{bus}V_{bus0}}(i_{dg0}\Delta V_{dg} + V_{dg0}\Delta i_{dg} + i_{qg0}\Delta V_{qg} \\ &+ V_{qg0}\Delta i_{qg} - V_{dr0}\Delta i_{dr} - i_{dr0}\Delta V_{dr} - i_{qr0}\Delta V_{qr} \\ &- V_{qr0}\Delta i_{qr}) - \frac{1}{C_{bus}V_{bus0}^2}(P_{g0} - P_{r0})\Delta V_{bus} \end{aligned} \tag{14}$$

where C_{bus} is the capacitance of the DC bus, V_{bus} is the voltage of the DC bus, and P_g and P_r are the power of grid side and rotor side respectively.

G. Interfacing Inductor Model

An interfacing inductor is connected in series with the GSC and the stator side to improve the output voltage waveform. Therefore, the inductor model can be expressed as

$$\begin{cases} L_g\frac{di_{dg}}{dt} + R_g i_{dg} - \omega_s i_{qg} = V_{dg} - V_{ds} \\ L_g\frac{di_{qg}}{dt} + R_g i_{qg} + \omega_s i_{dg} = V_{qg} - V_{qs} \end{cases} \tag{15}$$

The small-signal model of rotor-side filter can be expressed as

$$\begin{cases} \frac{d\Delta i_{dg}}{dt} = \frac{1}{L_g}(\Delta V_{dg} - \Delta V_{ds} - R_g\Delta i_{dg} + \omega_s\Delta i_{qg}) \\ \frac{d\Delta i_{qg}}{dt} = \frac{1}{L_g}(\Delta V_{qg} - \Delta V_{qs} - R_g\Delta i_{qg} - \omega_s\Delta i_{dg}) \end{cases} \tag{16}$$

where L_g is the interfacing inductor, and R_g is the parasitic resistance of the grid side filter.

H. Transmission Line Coupling Model

The transmission line of parallel DFIGs is usually inductive, the expression of the line equation is as follows.

$$\begin{cases} V_{ds} - V_{cnd} = R_{line}i_{dl} + L_{line}\frac{di_{dl}}{dt} - \omega_s L_{line} i_{ql} \\ V_{qs} - V_{cnq} = R_{line}i_{ql} + L_{line}\frac{di_{ql}}{dt} + \omega_s L_{line} i_{dl} \end{cases} \tag{17}$$

The output current connected to the grid side is expressed as follows

$$\begin{cases} i_{dl} = i_{ds1} + i_{dg1} + i_{ds2} + i_{dg2} \\ i_{ql} = i_{qs1} + i_{qg1} + i_{qs2} + i_{qg2} \end{cases} \tag{18}$$

Therefore, the small-signal model of the coupling parts between DFIGs can be expressed as

$$\begin{cases} \frac{d\Delta i_{dl}}{dt} = -\frac{R_{line}}{L_{line}}(\Delta i_{ds1} + \Delta i_{dg1} + \Delta i_{ds2} + \Delta i_{dg2}) \\ \qquad + \omega_s(\Delta i_{qs1} + \Delta i_{qg1} + \Delta i_{qs2} + \Delta i_{qg2}) + \frac{1}{L_{line}}\Delta V_{ds} \\ \frac{d\Delta i_{ql}}{dt} = -\frac{R_{line}}{L_{line}}(\Delta i_{qs1} + \Delta i_{qg1} + \Delta i_{qs2} + \Delta i_{qg2}) \\ \qquad - \omega_s(\Delta i_{ds1} + \Delta i_{dg1} + \Delta i_{ds2} + \Delta i_{dg2}) + \frac{1}{L_{line}}\Delta V_{qs} \end{cases} \tag{19}$$

where i_{dl} and i_{ql} are transmission line currents of d and q axis, which is the coupling variable, L_{line} is the inductance of the transmission line, R_{line} is the resistance of the transmission line, V_{cnd} and V_{cnq} are constant external busbar voltages of d and q axis, and the subscript with 1, 2 is the serial number of the parallel DFIGs.

According to the above analysis, the small signal linearization model of parallel DFIG can be expressed as

$$\frac{d\Delta X}{dt} = A \cdot \Delta X \tag{20}$$

$$\begin{aligned}\Delta X = [&\Delta\omega_{m1}\Delta i_{ds1}\Delta i_{qs1}\Delta i_{dr1}\Delta i_{qr1}\Delta x_{11}\Delta x_{21}\Delta x_{31}\Delta x_{41}\\ &\Delta x_{51}\Delta x_{61}\Delta V_{bus1}\Delta i_{dg1}\Delta i_{qg1}\Delta\theta_{pll1}\Delta\omega_{m2}\Delta i_{ds2}\\ &\Delta i_{qs2}\Delta i_{dr2}\Delta i_{qr2}\Delta x_{12}\Delta x_{22}\Delta x_{32}\Delta x_{42}\Delta x_{52}\Delta x_{62}\\ &\Delta V_{bus2}\Delta i_{dg2}\Delta\theta_{pll2}\Delta i_{qg2}\Delta i_{dl}\Delta i_{ql}]^T\end{aligned}$$

where ΔX is the state variable of the system, and $A \in R^{32\times 32}$ is the linearized state space matrix.

III. Integrated Reference Region Analysis of Parallel DFIGs

For state-space equations, a BMS based small-signal stability solving method can be used to obtain the stability region of variable parameters, which is computationally effective [21].

If a matrix Y has the dimension p, the BMS $H(Y)$ has the dimension $q = \frac{1}{2}p(p-1)$ and the elements of the matrix can be expressed as [22]

$$h_{\alpha\beta,mn} = \begin{cases} -y_{\alpha n} & \text{if } m = \beta \\ y_{\alpha m} & \text{if } m \neq \alpha,\ n = \beta \\ y_{\alpha\alpha} + a_{\beta\beta} & \text{if } m = \alpha \text{ and } n = \beta \\ y_{\beta n} & \text{if } m = \alpha \text{ and } n \neq \beta \\ -y_{\beta\alpha} & \text{if } n = \alpha \\ 0 & \text{if others} \end{cases} \tag{21}$$

where $\alpha\beta$ $(\alpha = 2, ..., p; \beta = 1, ..., \alpha - 1)$ are row labels and mn $(m = 2, ..., p; n = 1, ..., m - 1)$ are column labels. For instance, the BMS of a 3-dimension matrix Y is

$$H(Y) = \begin{bmatrix} y_{11}+y_{22} & y_{23} & -y_{13} \\ y_{32} & y_{11}+y_{33} & y_{12} \\ -y_{31} & y_{21} & y_{22}+y_{33} \end{bmatrix} \tag{22}$$

For state equations (20), the state matrix can be rewritten as follows

$$A(k) = A_0 + \sum_{i=1}^{l} k_i A_i \tag{23}$$

where A_0 is the nominal-value matrix that represents the reference value of a certain stable state, k_i is the parameter of the system, A_i is the variable parameter-location matrix that represents the distribution of the variable parameter in state matrix, l is the number of variable parameters.

Hence, the stability region for parameter k_i of the system in (20) can be expressed as

$$|\Delta k_i| = |k_i - k_{i0}| < \Gamma_0 \tag{24}$$

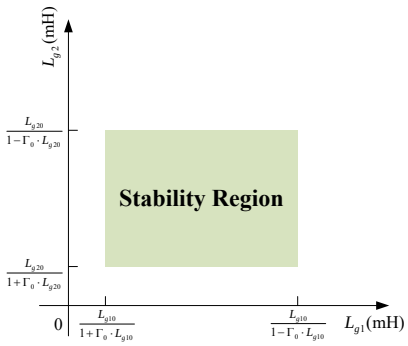

Fig. 6. Small-signal stability region of interfacing inductors

where

$$\begin{cases} \Gamma_0 = \min(\Gamma_1, \Gamma_2) \\ \Gamma_1 = \frac{1}{\rho\{\sum_{i=1}^{l} \left|A_i\cdot(A_0)^{-1}\right|_{abs}\}} \\ \Gamma_2 = \frac{2}{\rho\{\sum_{i=1}^{l} \left|H(A_i)[H(A_0)]^{-1}\right|_{abs}\}} \end{cases} \tag{25}$$

where ρ is the spectral radius of the matrix, $|\ |_{abs}$ is the matrix that every element is absolute value, and $H(\ )$ is the BMS.

If all the variable parameters k_i vary inside the bound Γ_0, the system remains stable.

According to (23), the lineraized matrix of (20) can be decomposed into A_0, A_1 and A_2. Let $k_1 = 1/L_{g1}$ and $k_2 = 1/L_{g2}$. The small-signal stability region can be calculated from (25) as

$$\begin{cases} \frac{L_{g10}}{1+\Gamma_0\cdot L_{g10}} < L_{g1} < \frac{L_{g10}}{1-\Gamma_0\cdot L_{g10}} \\ \frac{L_{g20}}{1+\Gamma_0\cdot L_{g20}} < L_{g2} < \frac{L_{g20}}{1-\Gamma_0\cdot L_{g20}} \end{cases} \tag{26}$$

The corresponding stability region is shown in Fig. 6.

Traditional interfacing inductor design for DFIG can be expressed as [4]

$$\begin{cases} i_{GSC\_\max} = \frac{P_s}{3V_s} \\ L_g = \frac{\sqrt{3}V_{bus}}{12P_s f_{sw} i_{GSC\_\max}\xi} \end{cases} \tag{27}$$

where $i_{GSC\_\max}$ is the maximum output current of GSC, P_s is the maximum rotor active power, f_{sw} is the switching frequency of GSC and ξ is the designed allowable current ripple.

The smaller allowable current ripple, the better the output current quality is. Accordingly, the greater the interfacing inductor is required. Under normal conditions, the interfacing inductor is limited to 20%-40% of the nominal peak current [23]. Besides, the selection of the inductor is in relation with the system loss at the selected switching frequency. Around 15%-20% of the maximum allowable current ripple is usually selected [24].

Therefore, for lower allowable current ripple considerations, the traditional design region for two parallel DFIGs' interfacing inductors can be expressed as

$$\begin{cases} L_{g1} \geq \frac{\sqrt{3}V_{bus1}}{12P_{s1} f_{sw} i_{GSC\_\max 1}\cdot 15\%} \\ L_{g2} \geq \frac{\sqrt{3}V_{bus2}}{12P_{s2} f_{sw} i_{GSC\_\max 2}\cdot 15\%} \end{cases} \tag{28}$$

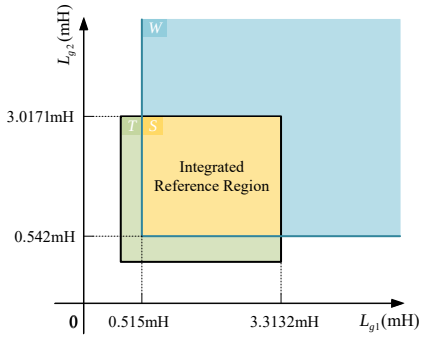

Fig. 7. simulation of the interfacing inductors' integrated reference region

Let T and W represents the region expressed by (26) and (28) respectively. The integrated reference region for two parallel DFIGs' interfacing inductors can be expressed as

$$S = T \cap W \tag{29}$$

IV. Simulations Results

In this section, two typical 2-MW DFIGs are modeled. The simulation model structure shown in Fig. 1 is implemented in the Matlab/simulink. A wind speed of $7.5\mathrm{m/s}$ is assumed. The DC bus voltage is set to 1150V. The maximum slip is 1/3. The rated stator voltage is set to 690V. The switching frequency is 10 kHz. For precise control of the electromagnetic torque, the rotor reference current of d axis is given to zero. Similarly, to ensure that the reactive power exchanged between the grid-side converter and DFIG is 0, the reference grid-side current of the q axis is set to 0. All the controller and the system parameters are given in the appendix A and B respectively.

According to (25), Γ_0 can be calculated as 2198.2, the small-signal stability region T of L_{g1} and L_{g2} can be calculated as

$$\begin{cases} 0.2128\mathrm{mH} < L_{g1} < 3.3132\mathrm{mH} \\ 0.2114\mathrm{mH} < L_{g2} < 3.0171\mathrm{mH} \end{cases} \tag{30}$$

Similarly, the region W expressed by (28) can be calcualted as

$$\begin{cases} L_{g1} \geq 0.515\mathrm{mH} \\ L_{g2} \geq 0.542\mathrm{mH} \end{cases} \tag{31}$$

Therefore, combining (30) and (31), the integrated reference region for parallel DFIGs' interfacing inductors can be calculated as

$$\begin{cases} 0.515\mathrm{mH} \leq L_{g1} \leq 3.3132\mathrm{mH} \\ 0.542\mathrm{mH} \leq L_{g1} \leq 3.0171\mathrm{mH} \end{cases} \tag{32}$$

The integrated reference region of interfacing inductors is displayed in Fig. 7. The green region, yellow region and blue region represent the region $T \cap \overline{W}$, region S and region $\overline{T} \cap W$, where $\overline{*}$ represents the region outside $*$.

Twenty two groups of simulations are carried out, with parallel DFIGs' interfacing inductors distributed in different regions. All the simulation results are shown in Table I. For each case, the DC bus voltage, DFIG output current,the d,q components of filtered GSC output currents and the active and reactive power of each DFIG are shown. To better illustrate the results, three typical cases are displayed as follows.

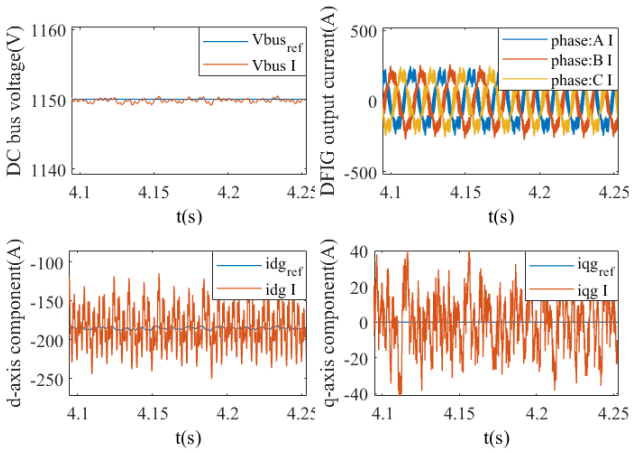

Fig. 8. The bus voltage/ output current waveforms of the first parallel DFIG under L_{g1}=0.12mH and L_{g2}=0.15mH

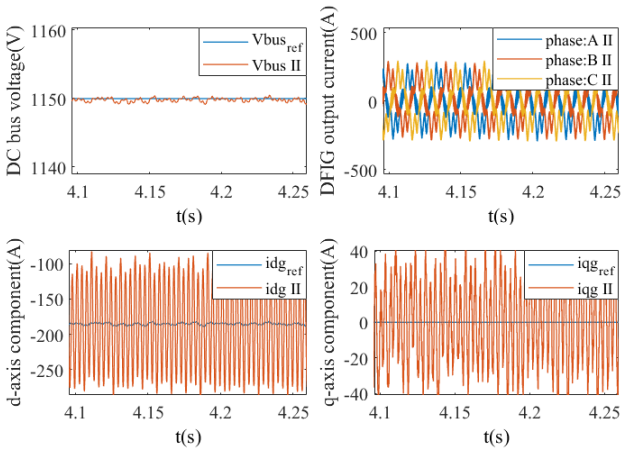

Fig. 9. The bus voltage/ output current waveforms of the second parallel DFIG under L_{g1}=0.12mH and L_{g2}=0.15mH

Case 1: Take $L_{g1} = 0.12mH$ and $L_{g2} = 0.15mH$. L_{g1} and L_{g2} are located inside the region $\overline{T} \cap \overline{W}$. According to theoretical analysis, the system is firstly unstable and obviously does not meet the requirements of current ripple. As seen from Fig. 8, Fig. 9 and Fig. 10, the d and q components of filtered GSC output currents begin to oscillate around the given reference value drastically. Although the DC bus voltage still remains around 1150V, the waveform quality of the output current of both DFIGs are very poor. The active and reactive power of the first DFIG oscillates drastically around 2 MW and 0 respectively. More seriously, the active and reactive power of the second DFIG has divergent oscillation. The results are in agreement with the analysis.

Case 2: Take $L_{g1} = 2.20mH$ and $L_{g2} = 1.90mH$. L_{g1} and L_{g2} are located inside the region S. According to theoretical analysis, the system is supposed to be stable and to meet the current ripple requirements. As seen from Fig. 11, Fig. 12 and Fig. 13, the d and q components of filtered GSC output currents are stable around the given reference value. The DC

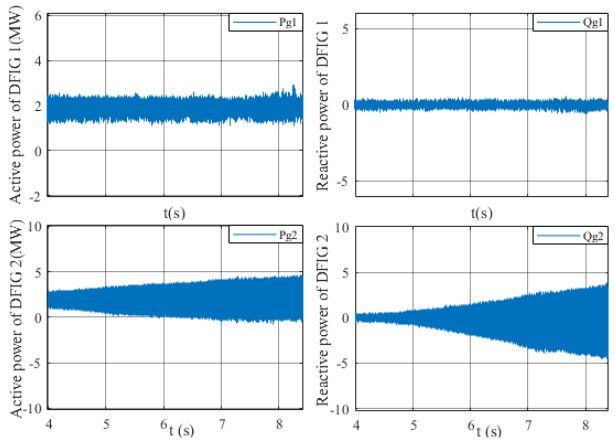

Fig. 10. The active and reactive power of parallel DFIGs under L_{g1}=0.12mH and L_{g2}=0.15mH

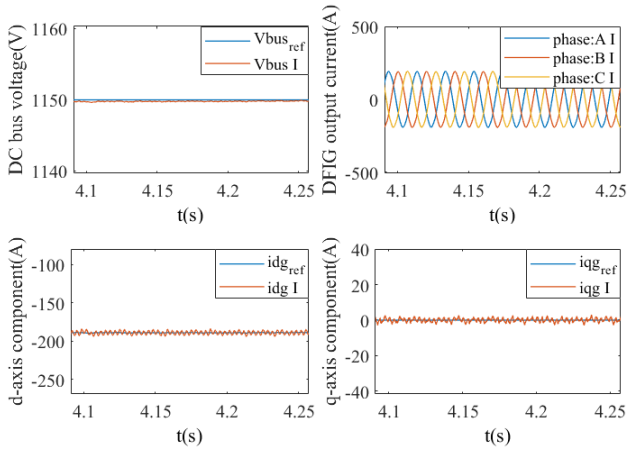

Fig. 11. The bus voltage/ output current waveforms of the first parallel DFIG under L_{g1}=2.2mH and L_{g2}=1.9mH

bus voltage remains around 1150V, the waveform quality of the output current of both DFIGs are perfect sinusoidal. The active and reactive power of both DFIGs remain 2 MW and 0 respectively. The system is stable. Besides, the current ripple of the first and the second DFIGs' are 3.514% and 4.280% which meets the current ripple requirements.

Case 3: Take $L_{g1} = 3.20mH$ and $L_{g2} = 3.30mH$. Both L_{g1} and L_{g2} are located inside the region $\overline{T} \cap W$. According to theoretical analysis, the system is firstly unstable. Although it is inside the traditional design-requirement region W, it is meaningless to calculate the current ripple for a unstable status and it obviously does not meet the requirements. As seen from Fig. 14, Fig. 15 and Fig. 16, the amplitudes of d and q components' oscillation are ever so large. Besides, the DC bus voltage and the ouput currents of DFIGs oscillate drastically as well. Same with the active and reactive power of both DFIGs. The system is unstable. The results are in agreement with the analysis.

For another possibility that located inside the region $T \cap \overline{W}$, case 10-11 show that although the system can maintain stability, it can not meet the ripple requirements.

From the analysis and simulation results, it can be seen that

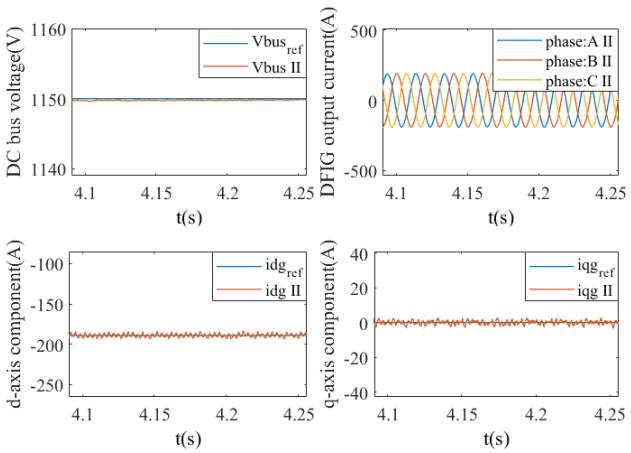

Fig. 12. The bus voltage/ output current waveforms of the second parallel DFIG under L_{g1}=2.2mH and L_{g2}=1.9mH

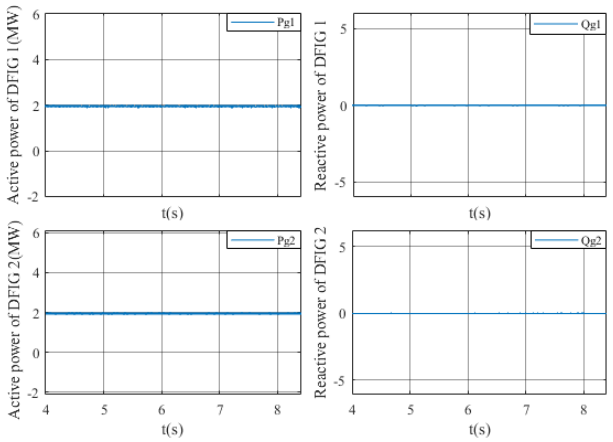

Fig. 13. The active and reactive power of parallel DFIGs under L_{g1}=2.2mH and L_{g2}=1.9mH

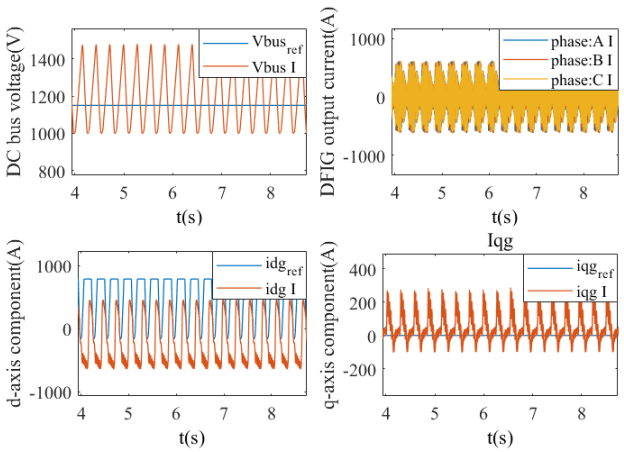

Fig. 14. The bus voltage/ output current waveforms of the first parallel DFIG under L_{g1}=3.2mH and L_{g2}=3.3mH

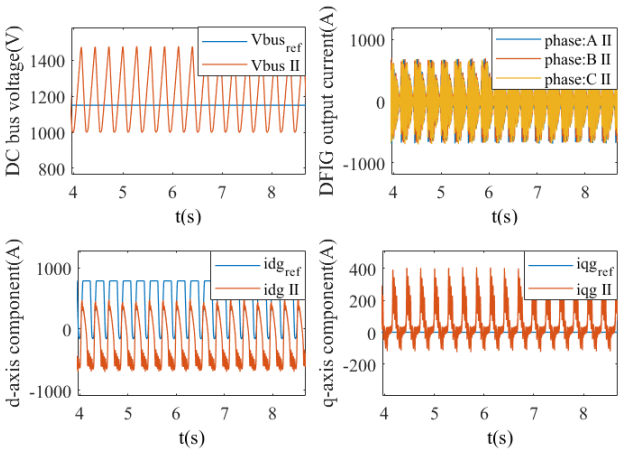

Fig. 15. The bus voltage/ output current waveforms of the second parallel DFIG under L_{g1}=3.2mH and L_{g2}=3.3mH

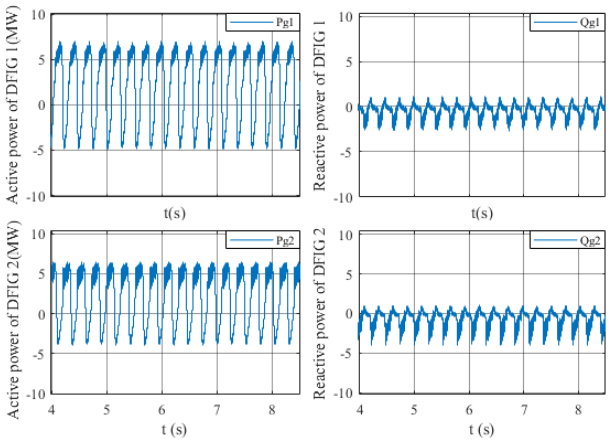

Fig. 16. The active and reactive power of parallel DFIGs under L_{g1}=3.2mH and L_{g2}=3.3mH

the traditional design of interfacing inductors can meet the requirements of current ripple to a certain extent indeed. As the current ripple requirement increases, the inductor increases accordingly, resulting to the location in region $\overline{S} \cap W$, where the small-signal instability is more prone to occur. Thus, depending on the traditional design requirements alone is not enough to ensure the stable operation of the system.

The rest simulation results can be seen from Table I, where 'o' represents oscillation and 's' represents stable for the state. Table I also displays the current ripple of each simulation case in percentage terms with '*' representing the corresponding current ripple that is meaningless for calculation. In case 1, 6, 7, 8, 17, 18, 20, 21, the inductors are evenly distributed in region $\overline{T} \cap \overline{W}$, where neither of the small-signal stability nor the current ripple meet the criteria. In case 3, 22, the inductors are distributed in region $\overline{T} \cap W$, where the inductors locate inside the traditional design-requirement region, but the system is unstable. In case 5, the inductors are in region $T \cap \overline{W}$, where the system is stable, but does not meet the ripple criteria. The simulation results show that the proposed integrated reference region for the design of interfacing inductor is instructive and of great significance for ensuring system's small-signal stability.

TABLE I
DIFFERENT INTERFACING INDUCTORS' SIMULATION RESULTS

case	L_{g1}	L_{g2}	ξ_1	ξ_2	state
1	0.12mH	0.15mH	*	*	o
2	2.20mH	1.90mH	3.514%	4.280%	s
3	3.20mH	3.30mH	*	*	o
4	0.10mH	0.10mH	*	*	o
5	0.10mH	0.30mH	*	*	o
6	0.12mH	2.31mH	*	*	o
7	0.15mH	3.00mH	*	*	o
8	0.17mH	3.22mH	*	*	o
9	0.31mH	0.10mH	*	*	o
10	0.31mH	0.33mH	24.938%	24.643%	s
11	0.41mH	0.47mH	18.856%	17.303%	s
12	1.05mH	1.05mH	7.363%	7.745%	s
13	1.17mH	2.25mH	6.608%	3.614%	s
14	1.51mH	0.76mH	5.120%	10.701%	s
15	2.36mH	2.95mH	3.276%	2.757%	s
16	2.40mH	1.41mH	3.221%	5.768%	s
17	2.20mH	0.10mH	*	*	o
18	3.20mH	0.15mH	*	*	o
19	3.20mH	3.00mH	2.416%	2.771%	s
20	3.40mH	0.14mH	*	*	o
21	5.00mH	0.10mH	*	*	o
22	3.90mH	4.10mH	*	*	o

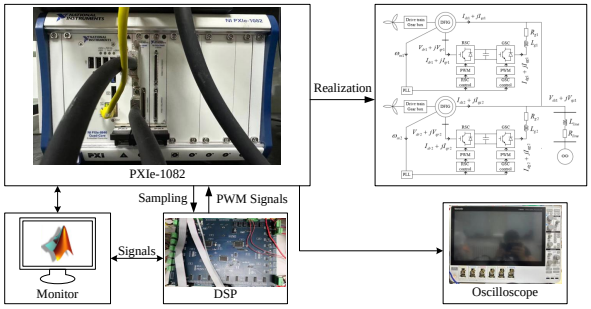

Fig. 17. The structure of HIL

V. Experimental Results

In order to verify the validity of the proposed integrated reference region for DFIGs' interfacing inductors, a hardware-in-the-loop (HIL) model of wind turbines based parallel DFIGs is built in this section. The structure of HIL is shown in Fig. 14, where the switching frequency is set to 10KHz. The Matlab simulation and control program are downloaded from the monitor to PXIe-1082 and digital signal processor (DSP). The DSP samples from the PXIe-1082 and generates PWM signals for it. An oscilloscope is connected to observe the waveform of the test system. Twenty groups of experiments are carried out, with parallel DFIGs' interfacing inductors distributed in different regions. All the simulation results are shown in Table II, which includes the state for parallel DFIGs' system and the current ripples in percentage terms. Three typical groups of experimental data and analysis are presented below.

Group 1: Take $L_{g1} = 0.11mH$ and $L_{g2} = 0.14mH$. L_{g1} and L_{g2} are located inside the region $\overline{T} \cap \overline{W}$. According to the theoretical analysis, the system is supposed to be unstable. As seen from Fig. 18 and Fig. 19, the first DFIG's d and q components of filtered GSC output currents oscillate around the reference value drastically. The DC bus voltage remains

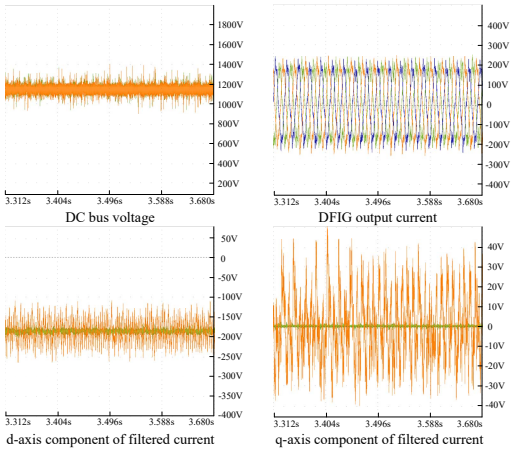

Fig. 18. The experiment waveforms of the first parallel DFIG under L_{g1}=0.11mH and L_{g2}=0.14mH

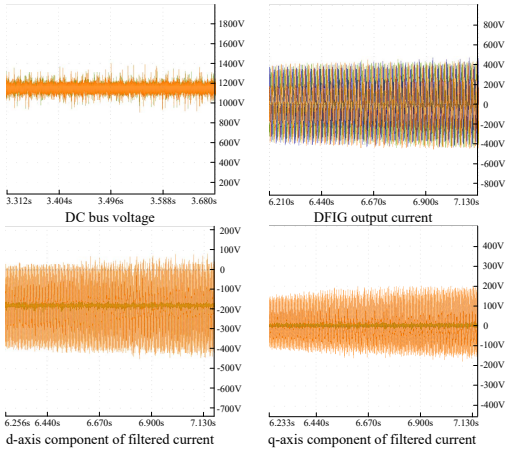

Fig. 19. The experiment waveforms of the second parallel DFIG under L_{g1}=0.11mH and L_{g2}=0.14mH

around the reference value generally. The waveform quality of the DFIG's output current is terribly poor. The second DFIG's DC bus voltage remains around the reference value. However, the d and q components diverge over time. Same with the output current. Thus, the parallel DFIGs' system is unstable, which verifies the analysis.

Group 2: Take $L_{g1} = 2.30mH$ and $L_{g2} = 2.00mH$. L_{g1} and L_{g2} are located inside the integrated reference region S. According to the theoretical analysis, the system is supposed to be stable and to meet the ripple requirements. As seen from Fig. 20 and Fig. 21, the first DFIG's d and q components of filtered GSC output currents remain around the reference value stably with almost no fluctuation. The output current's waveform is in high quality, whose current ripple is 3.361% within demand through measurement and calculation. The DC bus voltage is stable as well. The second DFIG's d and q components of filtered currents remains around reference value as well. Same with the DC bus voltage. The output current ripple is 4.066% within demand through measurement and calculation. Thus, the parallel DFIGs' system is stable and meets the traditional design requirements, which verifies the analysis.

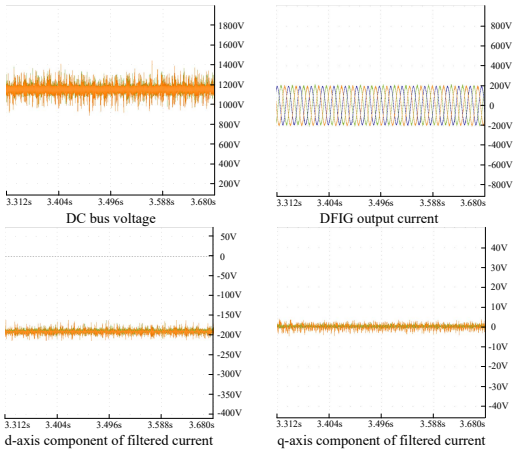

Fig. 20. The experiment waveforms of the first parallel DFIG under L_{g1}=2.30mH and L_{g2}=2.00mH

Group 3: Take $L_{g1} = 4.10mH$ and $L_{g2} = 4.40mH$. L_{g1} and L_{g2} are located inside the traditional design-requirement region $\overline{T \cap W}$. According to the theoretical analysis, the system is supposed to be unstable. As seen from Fig. 22 and Fig. 23, both the first and the second DFIGs' DC bus voltage oscillate severely. Moreover, the DFIGs' output currents are apparently unstable. The d and q components of filtered GSC output currents is in severe instability as well. Thus, the parallel DFIGs' system is unstable, which verifies the analysis.

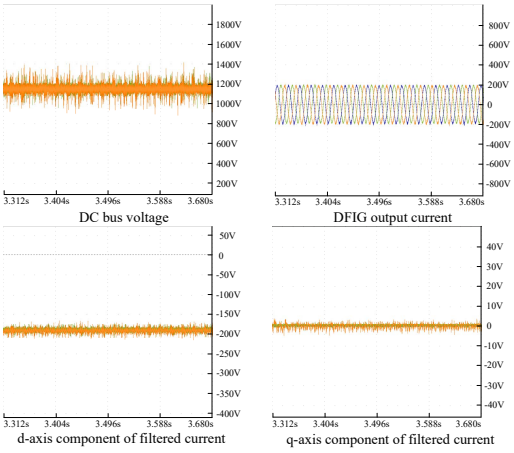

Fig. 21. The experiment waveforms of the second parallel DFIG under L_{g1}=2.30mH and L_{g2}=2.00mH

VI. Conclusion

This paper proposes an integrated reference region for parallel DFIGs' interfacing inductors. Firstly, a particular state-space model of parallel DFIGs based on wind turbines is proposed. It is mainly used for the analysis of parallel DFIGs' operation in distributed wind farms and considers the transmission line's coupling. Next, the interfacing inductor's integrated

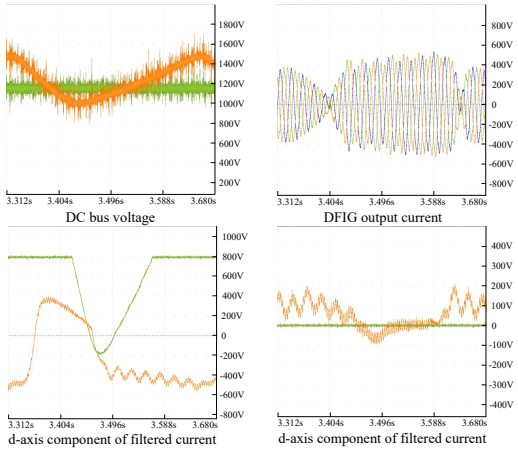

Fig. 22. The experiment waveforms of the first parallel DFIG under L_{g1}=4.10mH and L_{g2}=4.40mH

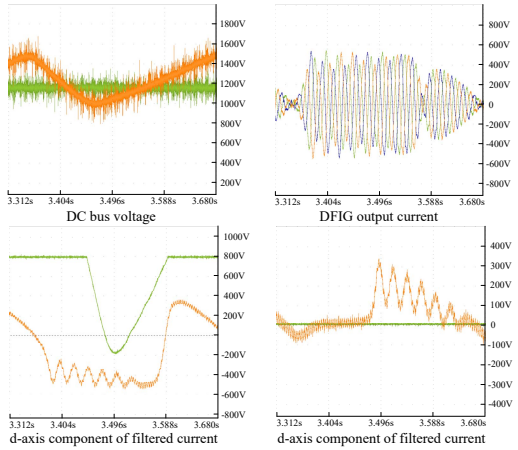

Fig. 23. The experiment waveforms of the second parallel DFIG under L_{g1}=4.10mH and L_{g2}=4.40mH

TABLE II
DIFFERENT INTERFACING INDUCTORS' EXPERIMENTAL RESULTS

case	L_{g1}	L_{g2}	ξ_1	ξ_2	state
1	0.11mH	0.14mH	*	*	o
2	2.30mH	2.00mH	3.451%	4.177%	s
3	4.10mH	4.40mH	*	*	o
4	0.08mH	0.08mH	*	*	o
5	0.08mH	0.25mH	*	*	o
6	0.10mH	2.40mH	*	*	o
7	0.15mH	3.00mH	*	*	o
8	0.20mH	3.20mH	*	*	o
9	0.30mH	0.08mH	*	*	o
10	0.30mH	0.35mH	27.779%	24.334%	s
11	0.45mH	0.41mH	18.286%	20.831%	s
12	1.00mH	1.07mH	7.831%	7.724%	s
13	1.15mH	2.20mH	6.822%	3.796%	s
14	1.54mH	0.73mH	5.224%	11.139%	s
15	2.36mH	2.91mH	3.557%	2.894%	s
16	2.70mH	1.35mH	2.963%	6.124%	s
17	3.20mH	2.95mH	2.539%	2.856%	s
18	3.35mH	0.18mH	*	*	o
19	5.00mH	0.20mH	*	*	o
20	3.75mH	3.80mH	*	*	o

reference region is obtained through BMS on the basis of traditional current ripple requirements. Both the simulation and experimental results prove the shortcomings of the traditional design method in guaranteeing system's small-signal stability and the proposed region's advantage in solving problems of current ripple and small-signal stability, which can provide a new method for interfacing inductors' design.

APPENDIX A
CONTROLLER PARAMETERS

Parameters	Values	Parameters	Values
ki_{id1}	491.5995	ki_{id2}	490.9273
kp_{id1}	0.5771	kp_{id2}	0.5865
ki_{v1}	-10000	ki_{v2}	-10000
kp_{v1}	-5000	kp_{v2}	-5000
ki_{idg1}	56.8489	ki_{idg2}	57.2124
kp_{idg1}	0.3016	kp_{idg2}	0.3155
ki_{iqg1}	56.8489	ki_{iqg2}	57.2124
kp_{iqg1}	0.3016	kp_{iqg2}	0.3155
ki_{pll1}	800	ki_{pll2}	800
kp_{pll1}	0.2	kp_{pll2}	0.2

APPENDIX B
SYSTEM PARAMETERS

Parameters	Values	Parameters	Values
Switching frequency	10kHz	Rotor inductance	2.6mH
Power rating	2MW	Line resistance	0.1Ω
Rated stator voltage	690V	Line inductance	5mH
Stator frequency	50Hz	DC bus voltge referred to stator	1150V
Rated stator current	1760A	Rotational inertia	$63.5\mathrm{Kg}\cdot\mathrm{m}^2$
Pole pair	2	Damping ratio	0.001
Stator/rotor turns ratio	1/3	Gearbox ratio	100
Rated rotor voltage	2070V	Radio of blades	42m
Maximum s1ip	1/3	Air density	$1.225\mathrm{Kg}/\mathrm{m}^3$
Stator resistance	0.0026Ω	Pitch angle	0
Leakage inductance (stator and rotor)	0.087mH	DC bus capacitance	0.08F
Magnetizing inductance	2.5mH	interfacing inductor	400μH
Rotor resistance referred to stator	2.9mΩ	Rotor-side filter resistance	0.0075Ω
Stator inductance	2.6mH	σ	0.0661

REFERENCES

[1] Global Wind Energy Council, 'Global Wind Report 2023', Accessed: March27. [Online] Available: https://gwec.net/globalwindreport2023/
[2] A. Lazar and S. M. Kotian, "Stability Analysis of a Grid-Connected DFIG Operating in Sub-synchronous and Super-synchronous Conditions," in *2022 IEEE International Power and Renewable Energy Conference (IPRECON)*, 2022, pp. 1-6.
[3] P. Kanjiya, B. B. Ambati and V. Khadkikar, "A Novel Fault-Tolerant DFIG-Based Wind Energy Conversion System for Seamless Operation During Grid Faults," *IEEE Trans. Power Syst.*, vol. 29, no. 3, pp. 1296-1305, May. 2014.
[4] N. K. Swami Naidu and B. Singh, "Doubly Fed Induction Generator for Wind Energy Conversion Systems With Integrated Active Filter Capabilities," *IEEE Trans Ind. Informat.*, vol. 11, no. 4, pp. 923-933, Aug. 2015.
[5] S. Jayalath and M. Hanif, "CL-filter design for grid-connected CSI," Proc. IEEE 13th Braz. Power Electron. Conf., 1st Southern Power Electron. Conf., Fortaleza, Brazil, 2015, pp. 1–6.
[6] S. Jayalath and M. Hanif, "Generalized LCL-Filter Design Algorithm for Grid-Connected Voltage-Source Inverter," *IEEE Trans. Ind. Electron.*, vol. 64, no. 3, pp. 1905-1915, March 2017
[7] R. Peña-Alzola, M. Liserre, F. Blaabjerg, M. Ordonez, and Y. Yang, "LCL-filter design for robust active damping in grid-connected converters," *IEEE Trans. Ind. Informat.*, vol. 10, no. 4, pp. 2192–2203, Nov. 2014
[8] C. Xie, K. Li, J. Zou and J. M. Guerrero, "Passivity-Based Stabilization of LCL-Type Grid-Connected Inverters via a General Admittance Model," *IEEE Trans. Power Electron.*, vol. 35, no. 6, pp. 6636-6648, June 2020

[9] A. Akhavan, H. R. Mohammadi, J. Vasquez, and J. M. Guerrero, "Passivity-based design of plug-and-play current controlled grid-connected inverters," *IEEE Trans. Power Electron.*, vol. 35, no. 2, pp. 2135–2150, Feb. 2020.
[10] J. Wang, J. D. Yan, L. Jiang, and J. Zou, "Delay-dependent stability of single-loop controlled grid-connected inverters with LCL filters," *IEEE Trans. Power Electron.*, vol. 31, no. 1, pp. 743–757, Jan. 2016.
[11] Y. Song and F. Blaabjerg, "Overview of DFIG-Based Wind Power System Resonances Under Weak Networks," *IEEE Trans. Power Electron.*, vol. 32, no. 6, pp. 4370-4394, June 2017
[12] B. Hu, H. Nian, M. Li and Y. Xu, "Impedance Characteristic Analysis and Reshaping Method of DFIG System Based on DPC Without PLL," *IEEE Trans. Ind. Electron.*, vol. 68, no. 10, pp. 9767-9777, Oct. 2021
[13] Y. Chen et al., "Reduced-Order System Frequency Response Modeling for the Power Grid Integrated With the Type-II Doubly-Fed Variable Speed Pumped Storage Units," *IEEE Trans. Power Electron.*, vol. 37, no. 9, pp. 10994-11006, Sept. 2022
[14] H. A. Mohammadpour and E. Santi, "Modeling and Control of Gate-Controlled Series Capacitor Interfaced With a DFIG-Based Wind Farm," *IEEE Trans. Ind. Electron.*, vol. 62, no. 2, pp. 1022-1033, Feb. 2015
[15] Z. Xie, Z. Xu, X. Zhang, S. Yang and L. Wang, "Improved Power Pulsation Suppression of DFIG for Wind Shear and Tower Shadow Effects," *IEEE Trans. Ind. Electron.*, vol. 64, no. 5, pp. 3672-3683, May 2017
[16] Z. Miao, "Impedance-model-based SSR analysis for Type 3 wind generator and series-compensated network," *IEEE Trans. Energy Convers.*, vol. 27, no. 4, pp. 984–991, Dec. 2012.
[17] B. Hu, H. Nian, J. Yang, M. Li and Y. Xu, "High-Frequency Resonance Analysis and Reshaping Control Strategy of DFIG System Based on DPC," *IEEE Trans. Power Electron.*, vol. 36, no. 7, pp. 7810-7819, July 2021
[18] R. Liu, J. Yao, X. Wang, P. Sun, J. Pei and J. Hu, "Dynamic Stability Analysis and Improved LVRT Schemes of DFIG-Based Wind Turbines During a Symmetrical Fault in a Weak Grid," *IEEE Trans. Power Electron.*, vol. 35, no. 1, pp. 303-318, Jan. 2020
[19] X. Fang, J. Yao, R. Liu, Y. Zhao, P. Sun and S. Huang, "Small-Signal Stability Analysis and Current Control Reference Optimization Algorithm of DFIG-Based WT During Asymmetric Grid Faults," *IEEE Trans. Power Electron.*, vol. 36, no. 7, pp. 7750-7768, July 2021
[20] J. Hu, B. Wang, W. Wang, H. Tang, Y. Chi and Q. Hu, "Small Signal Dynamics of DFIG-Based Wind Turbines During Riding Through Symmetrical Faults in Weak AC Grid," *IEEE Trans. Energy Convers.*, vol. 32, no. 2, pp. 720-730, June 2017.
[21] M. C. Pulcherio, M. S. Illindala and R. K. Yedavalli, "Robust Stability Region of a Microgrid Under Parametric Uncertainty Using Bialternate Sum Matrix Approach," *IEEE Trans. Power Syst.*, vol. 33, no. 5, pp. 5553-5562, Sept. 2018.
[22] W. Govaerts, B. Sijnave, Matrix manifolds and the Jordan structure of the bialternate matrix product, *Linear Algebra and its Applications*, Volume 292, Issues 1–3, 1999, Pages 245-266, ISSN 0024-3795
[23] T. Wang, C. Chen, T. Liu, Z. Chao and S. Duan, "Current Ripple Analysis of Three-Phase Vienna Rectifier Considering Inductance Variation of Powder Core Inductor," *IEEE Trans. Power Electron.*, vol. 35, no. 5, pp. 4568-4578, May 2020.
[24] Y. Jiao and F. C. Lee, "LCL Filter Design and Inductor Current Ripple Analysis for a Three-Level NPC Grid Interface Converter," *IEEE Trans. Power Electron.*, vol. 30, no. 9, pp. 4659-4668, Sept. 2015.

Rui Wang (Member, IEEE) received the B.S. degree in electrical engineering and automation and the Ph.D.degree in power electronics and power drive from Northeastern University, Shenyang, China, in 2016 and 2021, respectively. He is currently an Associate Professor with Northeastern University. He has authored or coauthored more than 50 papers, authorized more than 20 invention patents His research interests include collaborative optimization of distributed generation and its stability analysis of electromagnetic timescale in cyber-energy syetem.

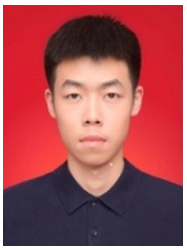

Xiaohan Yu received the B.S. degree in electrical engineering and automation from Northeastern University, Shenyang, China, in 2023. He is currently pursuing towards a Ph.D. degree in power electronics and power drive at Northeastern University. His research interest includes new energy power generation and small-signal stability analysis.

Qiuye Sun (Senior Member, IEEE) received the Ph.D. degree in 2007. Heis currently a Full Professor with Northeastern University and received Special Government Allowances from the State Council in China. He has authored or coauthored more than ten books or textbooks, more than 200 papers, and authorized more than 100 invention patents. His current research interests include optimization analysis technology of power distribution network, network control of energy Internet, integrated energy systems, and microgrids. He is currently an Associate Editor for the IEEE TRANSACTIONS ON NEURAL NETWORKS AND LEARNING SYSTEMS, IET Cyber-Physical Systems, CSEE Journal of Power and Energy Systems,and IEEE/CAA JOURNAL OF AUTOMATICA SINICA.

Dashuang Li received the B.Eng. and M.Sc. degrees in Electrical Engineering from Northeastern University, in China, in 2013 and 2015, respectively. He is currently pursuing a Ph.D. degree in Electrical Engineering at the Northeastern University, China. His research interests are collaborative optimization and stability analysis of distributed generation.

Yonghao Gui (Senior Member, IEEE) received the B.S. degree in automation from Northeastern University, Shenyang, China, in 2009, and the M.S. and Ph.D.degrees in electrical engineering from Hanyang University, Seoul, South Korea, in 2012 and 2017,respectively. From February 2017 to November 2018, he was with the Department of Energy Technology, Aalborg University, Aalborg, Denmark, as a Postdoctoral Researcher. Since December 2018, he has been with the Automation Control Section, Department of Electronic Systems, Aalborg University, Aalborg, Denmark, where he is currently an Assistant Professor. His research interests include control of power electronics in power systems,energy internet, and smart grids.

Dr. Gui was an Associate Editor for the IEEE TRANSACTION ON ENERGY CONVERSION, IEEE ACCESS,andInternational Journal of Control, Automation and Systems. He was the recipient of the IEEE Power & Energy Society General Meeting Best Conference Paper Award in 2019 and the IJCAS Academic Activity Award 2019.

Wang Peng (Fellow,IEEE) received the B.Sc.degree in electronic engineering from Xian Jiaotong University, Xian, China, in 1978, the M.Sc. degree from the Taiyuan University of Technology,Taiyuan,China,in 1987, and the M.Sc. and Ph.D. degrees in electrical engineering from the University of Saskatchewan, Saskatoon, SK, Canada, in 1995 and 1998, respectively. He is currently a Full Professor with the School of Electrical and Electronic Engineering, Nanyang Technological University, Singapore. His current re search interests include power system planning and operation,renewable energy planning,solar or electricity conversion system,and power system reliability analysis. He is an Associate Editor or Guest Editor-in Chief for or of the IEEE TRANSACTIONS ON SMART GRID, IEEE TRANSACTIONS ON POWER DELIVERY, Journal of Modern Power Systems and Clean Energy,and CSEE Journal of Power and Energy Systems.